AIAA JOURNAL
Vol. 42, No. 1, January 2004

Generalized Characteristic Boundary Conditions for Computational Aeroacoustics, Part 2

Jae Wook Kim* and Duck Joo Lee†
Korea Advanced Institute of Science and Technology, Daejeon 305-701, Republic of Korea

A previous paper introduced generalized characteristic boundary conditions for computational aeroacoustics (CAA), especially in the focus of far-field nonreflecting conditions. Strict wall boundary conditions are now developed on the basis of the generalized characteristics. True multidimensionality of the characteristic relations is guaranteed by maintaining entire terms of governing equations, which had been approximated virtually by local one-dimensional inviscid relations during the past two decades. Treating the transverse and viscous terms as source terms in the characteristic relations leads to an exact and simple formalism of wall boundary conditions. The formalism does not include any kind of extrapolation or assumption. The proposed inviscid and viscous wall boundary conditions are applied to typical CAA problems for verifying numerical accuracy in actual implementations. The computations are performed on nonorthogonal grids to exhibit the effect of multidimensionality on the solutions in acoustic fields. It is shown that the present results are in good agreement with analytic estimations and experimental data. This demonstrates the feasibility of the proposed wall boundary conditions for further practical CAA applications.

I. Introduction

VARIATIONS of characteristic boundary conditions have been used in many kinds of problems and research areas as mentioned in the previous paper.[1] Thompson[2,3] decomposed hyperbolic equations into quasi-linear characteristic wave modes of definite velocities in the direction normal to the computational boundary. The starting point of his analysis was the nonlinear Euler equations. The idea of his approach was that the amplitudes of outgoing waves could be defined entirely from the variables inside the computational domain, whereas those of incoming waves should be specified by proper characteristic boundary conditions. The characteristic boundary conditions were improved by Poinsot and Lele[4] and the authors[1] for Navier–Stokes computations and aeroacoustics with high-order numerical schemes. Especially, a fully conservative formalism of the characteristic relations in a generalized coordinate system was presented in Ref. 1, as well the introduction of the soft inflow conditions using the generalized characteristics.

At solid wall boundaries, it has been a usual practice to impose a condition to normal pressure gradient and to apply extrapolation techniques for all other variables. An improved strategy using ghost values of pressure to form boundary treatments was suggested by Tam and Dong,[5] Kurbatskii and Tam,[6] and Hixon[7] for computational aeroacoustics (CAA). In an effort to calculate density and velocity variations more accurately near the wall, the characteristic boundary conditions developed in Refs. 1–4 can be applied in the direction normal to the wall. The work in Refs. 1–4 was still based on local one-dimensional inviscid (LODI) analysis, which left a defect of the characteristic boundary conditions with the lack of true multidimensionality for the past two decades. The defect becomes more serious when skewed nonorthogonal grid meshes are used near the wall. The challenge remains to get rid of this kind of defect. Recently, Lockard and Morris[8] briefly demonstrated the way to fulfill the multidimensionality. Their idea was to include all of the transverse and viscous terms in the derivation of the characteristic relations. Although the idea was new and meant a lot in view of CAA, the paper was not devoted to the development of boundary conditions. They skipped additional conditions for viscous walls, even though the Navier–Stokes code was implemented. Their computations were performed on almost orthogonal grids, and the new advantage could not be exhibited. However, the idea merits attention, and now, more detailed procedures for developing the wall boundary conditions should be proposed, which is the objective of this paper.

To assist the development of the new idea, this paper presents a complete formalism of the solid wall boundary conditions using the generalized characteristic relations with true multidimensionality. It focuses on enhancing mathematical completeness of the wall boundary conditions for various cases: inviscid/viscous flows with stationary/pulsating bodies. The present work maintains the complete terms of the governing equations to lead to true multidimensionality, beyond the virtual LODI approximation being used until now. The transverse and viscous terms are treated as source terms in the characteristic relations. The formalism does not include any kind of extrapolation or assumption. In this way, a mathematically exact and simple formalism of the wall boundary conditions is derived. Numerical implementation of the derived wall boundary conditions requires little additional cost or complexity. The proposed wall boundary conditions are applied to two aeroacoustic problems to verify the numerical accuracy and performance in actual implementations for CAA. The calculations are carried out on skewed nonorthogonal grids to investigate the effects of true multidimensionality on the quality of solutions in acoustic fields.

The organization of the paper is as follows. In Sec. II, the governing equations transformed from Cartesian to the generalized coordinates are described. In Sec. III the numerical algorithms used, are introduced, especially, the high-order finite differences for evaluating the spatial derivatives. In Sec. IV, the detailed procedure of deriving the wall boundary conditions is presented. In Sec. V, the results of the computation are shown in comparison with analytic estimations and experimental data, and the numerical accuracy and performance of the proposed wall boundary conditions are validated. Finally, concluding remarks are made in Sec. VI.

II. Governing Equations

The governing equations are unsteady compressible Euler or Navier–Stokes equations. The flux vector form of the governing equations, transformed to the computational domain, may be

Received 10 December 2002; revision received 9 July 2003; accepted for publication 14 July 2003.

*BK21 Research Professor, Department of Aerospace Engineering, 373-1 Guseong, Yuseong; jwk@kaist.ac.kr.

†Professor, Department of Aerospace Engineering, 373-1 Guseong, Yuseong; djlee@mail.kaist.ac.kr. Member AIAA.

Table 1 Optimized coefficients for compact FDSs

Equation (3)	Equation (4)	Equation (5)	Equation (6)
$a_1 = 0.6511278808920836$	$a_{0,1} = -3.061503488555582$	$a_{1,0} = -0.5401943305881343$	$a_{2,0} = -0.1327404414078232$
$a_2 = 0.2487500014377899$	$a_{0,2} = 5.917946021057852$	$a_{1,2} = 0.8952361063034303$	$a_{2,1} = -0.6819452549637237$
$a_3 = 0.006144796612699781$	$a_{0,3} = 0.4176795271056629$	$a_{1,3} = 0.2553815577627246$	$a_{2,3} = 0.7109139355526556$
$\alpha = 0.5775233202590945$	$\alpha_{0,1} = 5.870156099940824$	$a_{1,4} = 0.007540293945825 39$	$a_{2,4} = 0.2459462758541114$
$\beta = 0.08953895334666784$	$\beta_{0,2} = 3.157271034936285$	$\alpha_{1,0} = 0.1663921564068434$	$a_{2,5} = 0.003965415751510620$
		$\alpha_{1,2} = 0.7162501763222718$	$\beta_{2,0} = 0.03447751898726934$
		$\beta_{1,3} = 0.08619830787164529$	$\alpha_{2,1} = 0.4406854601950040$
			$\alpha_{2,3} = 0.6055509079866320$
			$\beta_{2,4} = 0.08141498512587530$

expressed in generalized coordinates as

$$\frac{\partial \hat{\boldsymbol{Q}}}{\partial t} + \frac{\partial \hat{\boldsymbol{E}}}{\partial \xi} + \frac{\partial \hat{\boldsymbol{F}}}{\partial \eta} + \frac{\partial \hat{\boldsymbol{G}}}{\partial \zeta} = \hat{\boldsymbol{S}}_V \tag{1}$$

where the caret indicates the transformed properties. The vectors of the conservative variables and the Euler fluxes in the generalized coordinates may be represented as

$$\hat{\boldsymbol{Q}} = \boldsymbol{Q}/J, \qquad \hat{\boldsymbol{E}} = (\xi_x \boldsymbol{E} + \xi_y \boldsymbol{F} + \xi_z \boldsymbol{G})/J$$

$$\hat{\boldsymbol{F}} = (\eta_x \boldsymbol{E} + \eta_y \boldsymbol{F} + \eta_z \boldsymbol{G})/j, \qquad \hat{\boldsymbol{G}} = (\zeta_x \boldsymbol{E} + \zeta_y \boldsymbol{F} + \zeta_z \boldsymbol{G})/J \tag{2}$$

and $\hat{\boldsymbol{S}}_V$ is a source term that consists of the viscous flux derivatives for the Navier–Stokes equations but is zero for the Euler equations. All of the components of $\hat{\boldsymbol{S}}_V$ are fully described in the previous paper[1] and many textbooks. The vectors of the conservative variables and the Euler fluxes in Cartesian coordinates are given by

$$\boldsymbol{Q} = (\rho, \rho u, \rho v, \rho w, \rho e_t)^T$$

$$\boldsymbol{E} = \left(\rho u, \rho u^2 + p, \rho v u, \rho w u, (\rho e_t + p)u\right)^T$$

$$\boldsymbol{F} = \left(\rho v, \rho u v, \rho v^2 + p, \rho w v, (\rho e_t + p)v\right)^T$$

$$\boldsymbol{G} = \left(\rho w, \rho u w, \rho v w, \rho w^2 + p, (\rho e_t + p)w\right)^T$$

where the total energy per unit mass is defined as $e_t = p/[(\gamma - 1)\rho] + (u^2 + v^2 + w^2)/2$ and $\gamma = c_p/c_v$ is the ratio of specific heats. For air, $\gamma = 1.4$ in the present computation. In Eq. (2), the transformation Jacobian J and the grid metrics, $\xi_x, \ldots, \zeta_z$ are given by

$$J = 1/[x_\xi(y_\eta z_\zeta - y_\zeta z_\eta) + x_\eta(y_\zeta z_\xi - y_\xi z_\zeta) + x_\zeta(y_\xi z_\eta - y_\eta z_\xi)]$$

with

$$\begin{pmatrix} \xi_x & \xi_y & \xi_z \\ \eta_x & \eta_y & \eta_z \\ \zeta_x & \zeta_y & \zeta_z \end{pmatrix} = J \begin{pmatrix} y_\eta z_\zeta - y_\zeta z_\eta & z_\eta x_\zeta - z_\zeta x_\eta & x_\eta y_\zeta - x_\zeta y_\eta \\ y_\zeta z_\xi - y_\xi z_\zeta & z_\zeta x_\xi - z_\xi x_\zeta & x_\zeta y_\xi - x_\xi y_\zeta \\ y_\xi z_\eta - y_\eta z_\xi & z_\xi x_\eta - z_\eta x_\xi & x_\xi y_\eta - x_\eta y_\xi \end{pmatrix}$$

III. Numerical Algorithms

High-order finite difference schemes (FDSs) are used to evaluate the flux derivatives in the present computation on a structured grid. The main scheme is a pentadiagonal type of central compact FDSs.[9] It is a generalization of the seven-point stencil Padé scheme used on the interior nodes. It may be expressed as

$$\beta f'_{i-2} + \alpha f'_{i-1} + f'_i + \alpha f'_{i+1} + \beta f'_{i+2} = \frac{1}{h}\sum_{m=1}^{3} a_m (f_{i+m} - f_{i-m}) \tag{3}$$

where f_i is an objective function for the flux variables and f'_i is its space derivative at the ith node. The grid spacing h is a constant, independent of the index i in the computational domain, where all of the grid points are equally spaced. Equation (3) may be solved by inverting a pentadiagonal matrix. The matrix must be completed at the boundaries. Therefore, noncentral or one-sided formulations other than Eq. (3) are needed on the boundary and the near-boundary nodes.[9] These may be represented as follows:

For $i = 0$ (boundary node),

$$f'_0 + \alpha_{0,1} f'_1 + \beta_{0,2} f'_2 = \frac{1}{h}\sum_{\substack{m=0 \\ m\neq 0}}^{3} a_{0,m}(f_m - f_0) \tag{4}$$

For $i = 1$,

$$\alpha_{1,0} f'_0 + f'_1 + \alpha_{1,2} f'_2 + \beta_{1,3} f'_3 = \frac{1}{h}\sum_{\substack{m=0 \\ m\neq 1}}^{4} a_{1,m}(f_m - f_1) \tag{5}$$

For $i = 2$,

$$\beta_{2,0} f'_0 + \alpha_{2,1} f'_1 + f'_2 + \alpha_{2,3} f'_3 + \beta_{2,4} f'_4 = \frac{1}{h}\sum_{\substack{m=0 \\ m\neq 2}}^{5} a_{2,m}(f_m - f_2) \tag{6}$$

The coefficients in Eqs. (3–6) are listed in Table 1. They are optimized, as described in Refs. 9 and 10, to achieve maximum resolution characteristics with fourth-order accuracy [second-order in Eq. (4) for numerical stability]. Combined with the high-order FDSs in space, the classical fourth-order, four-stage Runge–Kutta scheme is used for marching the solutions in time.

High-order FDSs in space and time resolve a wider range of wave number or frequency than low-order schemes. However, even the present schemes do not resolve the highest wave number or frequency range effectively, and an adaptive nonlinear artificial dissipation model[11] is also used to remove the unwanted numerical oscillations that may develop from the unresolved range. In addition, an accurate and robust CAA calculation depends heavily on the suppression of any waves that may result from unwanted reflections on far-field boundaries. The previous work[1] was devoted to the far-field boundary conditions. The far-field boundary conditions were derived on the basis of the LODI approximation.[1–4] Multidimensionality has not been established for the far-field boundary conditions yet because it is quite difficult to specify any flow variable or its time derivative at the far field. The far-field boundary conditions based on the LODI approximation are still used in the present work. Therefore, the zonal boundary conditions proposed by Freund[12] are supplemented for enhancing the nonreflecting feature near the far-field boundaries.

IV. Generalized Characteristic Boundary Conditions for Solid Walls

This section presents an enhanced formalism of the generalized characteristic boundary conditions for solid walls. It can be derived from the characteristic relations that are obtained by transforming the governing equations into quasi-linear wave equations in the direction normal to the wall boundary. The derivation includes neither assumptions nor simplifications, which means the proposed

wall boundary conditions are mathematically exact. No kind of extrapolation or ghost point technique is considered in this approach. Numerical implementation would be quite straightforward. The detailed procedure is explained in the following subsections.

A. Transformation to Generalized Characteristic Form

The starting point of the analysis for deriving the wall boundary conditions is Eq. (1). Equation (1) can be transformed into a generalized characteristic form in the direction normal to the boundary, where ξ keeps a constant value. The transformed characteristic equation is a kind of quasi-linear wave equation with a source term. The resulting equation may be expressed as

$$\frac{\partial \boldsymbol{R}}{\partial t} + \boldsymbol{L} = \boldsymbol{S}_C \tag{7}$$

where $\boldsymbol{R}$ is the vector of characteristic variables and $\boldsymbol{L}$ is its convection term. Equation (7) is derived by the following two equations of identity associated with Eq. (2):

$$\delta \boldsymbol{R} = \underline{\boldsymbol{P}}^{-1}\delta \boldsymbol{Q}, \qquad \boldsymbol{L} \equiv \underline{\lambda}\frac{\partial \boldsymbol{R}}{\partial \xi} = \underline{\boldsymbol{P}}^{-1}\left(\xi_x \frac{\partial \boldsymbol{E}}{\partial \xi} + \xi_y \frac{\partial \boldsymbol{F}}{\partial \xi} + \xi_z \frac{\partial \boldsymbol{G}}{\partial \xi}\right)$$

where the underlines indicate matrices. The source term in Eq. (7) is related to the source term in Eq. (1), after some mathematics, as

$$\boldsymbol{S}_C = J\,\underline{\boldsymbol{P}}^{-1}\left\{\hat{\boldsymbol{S}}_V - \left[\boldsymbol{E}\frac{\partial}{\partial \xi}\left(\frac{\xi_x}{J}\right) + \boldsymbol{F}\frac{\partial}{\partial \xi}\left(\frac{\xi_y}{J}\right) + \boldsymbol{G}\frac{\partial}{\partial \xi}\left(\frac{\xi_z}{J}\right) + \frac{\partial \hat{\boldsymbol{F}}}{\partial \eta} + \frac{\partial \hat{\boldsymbol{G}}}{\partial \zeta}\right]\right\} \tag{8}$$

where $\hat{\boldsymbol{S}}_V$ disappears when the Euler equations are employed. The characteristic differential variables and the corresponding convection speeds are represented as

$$\delta \boldsymbol{R} = \left(\delta\rho - \frac{\delta p}{c^2}, \delta \tilde{W}, \delta \tilde{V}, \frac{\delta p}{\rho c} + \delta \tilde{U}, \frac{\delta p}{\rho c} - \delta \tilde{U}\right)^T$$

$$\underline{\lambda}(\text{diagonal}) = \left(U, U, U, U + c\sqrt{\xi_x^2 + \xi_y^2 + \xi_z^2}, U - c\sqrt{\xi_x^2 + \xi_y^2 + \xi_z^2}\right)^T \tag{9}$$

where c is speed of sound. Contravariant velocity in the direction normal to the boundary and its differential are given by

$$U = \xi_x u + \xi_y v + \xi_z w, \qquad \delta \tilde{U} = \tilde{\xi}_x \delta u + \tilde{\xi}_y \delta v + \tilde{\xi}_z \delta w$$

whereas the velocity differentials in the parallel direction are expressed as

$$\delta \tilde{V} = -\tilde{\xi}_x \delta v + \tilde{\xi}_y \delta u, \qquad \delta \tilde{W} = \tilde{\xi}_x \delta w - \tilde{\xi}_z \delta u$$

The tilde indicates a variable normalized by the amplitude of metric vector as given by

$$(\tilde{\xi}_x, \tilde{\xi}_y, \tilde{\xi}_z) = \frac{(\xi_x, \xi_y, \xi_z)}{\sqrt{\xi_x^2 + \xi_y^2 + \xi_z^2}} \tag{10}$$

The matrix $\underline{\boldsymbol{P}}^{-1}$ that transforms the conservative variables into the characteristic variables and its inverse matrix $\underline{\boldsymbol{P}}$ can diagonalize the flux-Jacobian matrices in the direction normal to the boundary, and the resulting diagonal terms become the convection speeds of the characteristic waves. The diagonalizing procedure is described precisely in Refs. 13 and 14. The transformation matrices and its constituting variables are given in the Appendix.

B. True Multidimensionality

Equation (7) represents the physical (entropy, vorticity, and acoustic) waves with different convection speeds in the direction normal to the boundary as expressed in Eq. (9). An advantage of using the characteristic equations is that the incoming and the outgoing waves can be classified easily by the signs of convection speeds. The characteristic boundary conditions deal with the incoming waves in that the physical information carried into computational domain cannot be calculated directly just by numerical differentiations. To simulate strict wall boundary conditions, the incoming waves should be corrected in relation to the outgoing waves that transport the physical information out of the domain. In addition, evaluation of the incoming waves should be associated with the source term in Eq. (7), which is very obvious in a mathematical sense.

The source term cannot be zero even in the simplest case with an inviscid flow on a uniform rectangular grid because the last two transverse terms in Eq. (8) survive. However, the source term has been neglected by applying the LODI approximation for the past two decades.[1–4] The LODI approximation has led to a lack of multidimensionality in that the transverse terms are not included at all. The present approach, just as Lockhard and Morris[8] did, maintains all of the source terms in the derivation of the wall boundary conditions for constructing the true multidimensionality. In this regard, Eq. (7) can be recast in terms of primitive variables as follows:

$$\frac{\partial \rho}{\partial t} + L_1 + \frac{\rho}{2c}(L_4 + L_5) = S_{C1} + \frac{\rho}{2c}(S_{C4} + S_{C5}) \tag{11}$$

$$\frac{\partial \tilde{U}}{\partial t} + \frac{1}{2}(L_4 - L_5) = \frac{1}{2}(S_{C4} - S_{C5}) \tag{12}$$

$$\frac{\partial \tilde{V}}{\partial t} + L_3 = S_{C3} \tag{13}$$

$$\frac{\partial \tilde{W}}{\partial t} + L_2 = S_{C2} \tag{14}$$

$$\frac{\partial p}{\partial t} + \frac{\rho c}{2}(L_4 + L_5) = \frac{\rho c}{2}(S_{C4} + S_{C5}) \tag{15}$$

Equations (11–15) are actually used to impose suitable values to the incoming convection terms L_i according to the boundary types. If the LODI approximation were to be applied, the right-hand sides of Eqs. (11–15) would be all zero, which is clearly incorrect. To simulate wall boundaries, Eqs. (12–14) are used to impose nopenetration with slip/no-slip conditions according to inviscid or viscous cases. The overall procedure of implementation is shown in the next subsection.

C. Overall Implementation Procedure

For practical application to actual computations, the detailed procedure for implementing the characteristic wall boundary conditions is summarized by the following steps:

1) All of the flux derivatives in Eq. (1) are evaluated by the high-order FDSs given by Eqs. (3–6) in the whole domain, including the boundary points. The normal-flux derivative $\partial \hat{\boldsymbol{E}}/\partial \xi$ on the boundary is used as an initial guess to be corrected next.

2) The initial guess of the characteristic convection term on the boundary is then evaluated by the following equation of identity:

$$\boldsymbol{L} = J\,\underline{\boldsymbol{P}}^{-1}\left\{\frac{\partial \hat{\boldsymbol{E}}}{\partial \xi} - \left[\boldsymbol{E}\frac{\partial}{\partial \xi}\left(\frac{\xi_x}{J}\right) + \boldsymbol{F}\frac{\partial}{\partial \xi}\left(\frac{\xi_y}{J}\right) + \boldsymbol{G}\frac{\partial}{\partial \xi}\left(\frac{\xi_z}{J}\right)\right]\right\}$$

3) The characteristic convection term on the boundary is then corrected by imposing the wall conditions to be described in the next subsections. Then, the new corrected characteristic convection term is represented by $\boldsymbol{L}^*$.

4) Finally, the normal-flux derivative term is then recalculated by the corrected characteristic convection term via the following

equation of identity:

$$\left(\frac{\partial \hat{\boldsymbol{E}}}{\partial \xi}\right)^{*} = \frac{1}{J}\,\underline{\boldsymbol{P}}\boldsymbol{L}^{*} + \left[\boldsymbol{E}\frac{\partial}{\partial \xi}\left(\frac{\xi_x}{J}\right) + \boldsymbol{F}\frac{\partial}{\partial \xi}\left(\frac{\xi_y}{J}\right) + \boldsymbol{G}\frac{\partial}{\partial \xi}\left(\frac{\xi_z}{J}\right)\right]$$

The new corrected normal-flux derivative term with the asterisk superscript is then returned to Eq. (1) for integrating the solutions in time.

This procedure is iterated in every stage of the time-marching steps. In this way, imposing the wall boundary conditions can be accomplished, and accurate numerical solutions can be guaranteed. The numerical implementation is simple and straightforward in that it needs just some additional operations only on the boundary points using ready-made matrices. The next subsections illustrate two kinds of wall boundary conditions: pulsating inviscid wall and stationary viscous wall to be used in Sec. V.

D. Pulsating Inviscid Wall

An inviscid wall exhibits no penetration of flow with the slip condition on it. This means the contravariant velocity $\tilde{U}$ that is normal to the wall should be zero or specified by a function of space and time if the wall behaves as an acoustic source. When the wall pulsates acoustically, the time derivative of the normal velocity $\mathrm{d}\tilde{U}/\mathrm{d}t$ should be also specified on the wall. For an inviscid wall located at the left boundary of the computational domain, the signs of the convection speeds indicate that the incoming wave is L_4 and the outgoing wave is given by L_5. Likewise, for the wall at the right boundary, the incoming wave is L_5, and the outgoing wave is given by L_4. As a result, from Eq. (12), the following equations can be derived to evaluate the incoming waves:

For the left-sided wall,

$$L_4^{*} = L_5 + S_{C4} - S_{C5} - 2\left.\frac{\mathrm{d}\tilde{U}}{\mathrm{d}t}\right|_{\text{wall}} \tag{16a}$$

For the right-sided wall,

$$L_5^{*} = L_4 - S_{C4} + S_{C5} + 2\left.\frac{\mathrm{d}\tilde{U}}{\mathrm{d}t}\right|_{\text{wall}} \tag{16b}$$

where the wall pulsation term $\mathrm{d}\tilde{U}/\mathrm{d}t = 0$ if the wall is stationary. In this way, the incoming convection term can be corrected by Eq. (16) and imposed into step 3 of the preceding subsection to establish the wall conditions with true multidimensionality.

Although the normal velocity component is specified, all of the momentum equations in Eq. (1) should be solved by integrating in time to get the parallel velocity components. In a mathematical sense, Eq. (16) satisfies the no-penetration condition exactly on the wall. However, a certain level of roundoff error may develop in the numerical integration. Therefore, it is required to refine the velocity for the normal component to be in perfect agreement with the specified value. Once the Cartesian velocity components are solved by the numerical integration of Eq. (1), the generalized (normal and parallel) velocity components can be obtained. Then, the following equation is used to correct the velocity with the exact value of the normal component $\tilde{U}^{*}$, while letting the parallel components $\tilde{V}$ and $\tilde{W}$ remain unchanged:

$$\begin{pmatrix} u^{*} \\ v^{*} \\ w^{*} \end{pmatrix} = \begin{pmatrix} \tilde{\xi}_x & \tilde{\xi}_y & \tilde{\xi}_z \\ \tilde{\xi}_y & -\tilde{\xi}_x & 0 \\ -\tilde{\xi}_z & 0 & \tilde{\xi}_x \end{pmatrix}^{-1} \begin{pmatrix} \tilde{U}^{*} \\ \tilde{V} \\ \tilde{W} \end{pmatrix}$$

where the asterisk superscript indicates the new corrected value, as earlier remarked. This process can clean up the machine error that might accumulate to be a considerable level through the time steps, which is, otherwise, unnecessary in a mathematical sense.

E. Stationary Viscous Wall

A viscous wall exhibits no-penetration of flow as well as no-slip condition on it. When the wall is stationary, all of the velocity components and their time derivatives should be zero. For the no-penetration conditions, Eq. (16) should be also applied to the viscous wall just like the inviscid case with zero wall pulsation terms. As a result, the following equations are used to evaluate the incoming waves according to the position of wall boundary:

For the left-sided wall,

$$L_4^{*} = L_5 + S_{C4} - S_{C5} \tag{17a}$$

For the right-sided wall,

$$L_5^{*} = L_4 - S_{C4} + S_{C5} \tag{17b}$$

In addition, from Eqs. (13) and (14), it can be found that $L_3 = S_{C3}$ and $L_2 = S_{C2}$ are satisfied because the parallel velocity components are also zero. In the meantime, the characteristic convection terms L_3 and L_2 are equal to zero, because their convection speeds are zero as shown in Eq. (9). Therefore, the following equations should be used additionally for the viscous wall:

$$L_2^{*} = L_3^{*} = 0 \tag{18}$$

$$S_{C2}^{*} = S_{C3}^{*} = 0 \tag{19}$$

The incoming convection terms can be corrected by Eqs. (17) and (18) and imposed in step 3 in Sec. IV.C to establish the wall conditions with true multidimensionality.

Now, Eq. (19) is to be used to complete the viscous wall conditions before the time integration of the governing equations. The viscous source term in Eq. (1) should be also corrected by Eqs. (8) and (19) as

$$\hat{\boldsymbol{S}}_V^{*} = \frac{1}{J}\,\underline{\boldsymbol{P}}\boldsymbol{S}_C^{*} + \left[\boldsymbol{E}\frac{\partial}{\partial \xi}\left(\frac{\xi_x}{J}\right) + \boldsymbol{F}\frac{\partial}{\partial \xi}\left(\frac{\xi_y}{J}\right) + \boldsymbol{G}\frac{\partial}{\partial \xi}\left(\frac{\xi_z}{J}\right) + \frac{\partial \hat{\boldsymbol{F}}}{\partial \eta} + \frac{\partial \hat{\boldsymbol{G}}}{\partial \zeta}\right] \tag{20}$$

Equation (20) shows that the no-penetration and no-slip conditions have an effect on the viscous flux derivatives, not only on the Euler flux derivatives. This process seems quite obvious, and it is newly proved in the present work. In addition, to calculate the viscosity effect more precisely, some artificial boundary conditions can be supplemented by using an idea of Tourrette[15] in the case of direct numerical simulation or large eddy simulation. After all of these corrections, only the continuity and energy equations in Eq. (1) are integrated in time for solving density and pressure, whereas the velocity components are set to zero.

V. Application to Actual Computations

In this section, the proposed wall boundary conditions are applied to the actual computations. The mathematical exactness and the numerical accuracy are investigated by solving the inviscid and viscous aeroacoustic benchmark problems that have analytic solutions and experimental data to be compared with the present results. Two kinds of problems are considered. One is simulating dipole sound fields in steady inviscid flows past an oscillating circular cylinder. The other also is simulating a dipole sound field, but generated by viscous flow past a stationary circular cylinder, which is famous for regular vortex shedding, that is, the von Kármán vortex street behind the cylinder (see Ref. 16). The present computations are performed in two dimensions rather than three dimensions to reduce the computational complexity and effort. The results of the computations are presented as follows.

A. Inviscid Flow past an Oscillating Cylinder

An inviscid flow past a circular cylinder is a steady flow without separation behind the cylinder, and it is close to the ideal or potential

flow in the low-Mach-number regime. When the cylinder oscillates acoustically up and down in the steady flow, it will generate a dipole sound field in the direction of the oscillation. Let the amplitude and the frequency of the oscillation be ε and ω, respectively, then the normal velocity can be expressed as $\tilde{U} = \varepsilon c_\infty \cos\phi \sin(\omega t)$ at the cylinder surface, where ϕ is measured from the axis of oscillation. In this problem, the axis of oscillation is equal to y axis; then it can be shown that $\cos\phi = \tilde{\xi}_y$ if the cylinder surface is on a line of constant ξ. Therefore, the time derivative of normal velocity is given by

$$\left.\frac{\mathrm{d}\tilde{U}}{\mathrm{d}t}\right|_{\text{wall}} = \varepsilon\omega c_\infty \tilde{\xi}_y \cos(\omega t) \tag{21}$$

which is imposed into Eq. (16) for implementing the wall boundary conditions of the oscillating cylinder. There exists an analytic solution when there is no mean flow.[17] The analytic solution for the sound pressure level (SPL) expressed by rms acoustic pressure $[p'(\boldsymbol{x}, t) = p(\boldsymbol{x}, t) - p_\infty]$ is given by

$$p'_{\text{rms}}(\boldsymbol{x}) = \overline{p'^2}^{\frac{1}{2}}(\boldsymbol{x}) = \frac{1}{\sqrt{2}}\varepsilon\rho_\infty c_\infty^2 \cos\phi \left|\frac{H_0'(\omega r/c_\infty)}{H_0''(\omega R/c_\infty)}\right|$$

where $H_0(z)$ is a zeroth-order Hankel function, $H_0'(z) = \mathrm{d}H_0/\mathrm{d}z$, r is distance from the center of cylinder, and R is the cylinder radius. The analytic solution is compared with the computed solutions to validate the numerical accuracy of the proposed boundary conditions.

The dipole sound fields are calculated for four different freestream Mach numbers: $M_\infty = 0$, 0.1, 0.2, and 0.3. Equation (1) without the viscous source term in two dimensions is solved for this computation. Except for the zero-Mach-number case, the steady mean solutions are achieved first with $\varepsilon = 0$ in Eq. (21), and the cylinder begins to oscillate afterward. The grid system used for this problem is shown in Fig. 1, where D is the cylinder diameter. The non-orthogonal grid meshes are generated by H topology. The number of grid meshes is 194×144. The meshes are clustered toward the cylinder, and the smallest mesh size is $\Delta x/D = \Delta y/D = 0.0225$. The grid metrics and Jacobian are evaluated by the numerical differentiations with Eqs. (3–6). Time step size is determined by the Courant–Friedrichs–Lewy (CFL) condition with the Courant number of 1.0. The number of iterations used to reach the steady mean solutions is 50,000, and the maximum value of the error residual $|p^{(n+1)} - p^{(n)}|/p^{(n)}$ falls below 1.0×10^{-7}, that is, an order of machine error. Once steady state is reached, the cylinder surface oscillates with $\varepsilon = 1.0 \times 10^{-4}$ and $\omega = 2\pi c_\infty/D$ during the time $t = 20D/c_\infty$, that is, 20 times the wave period.

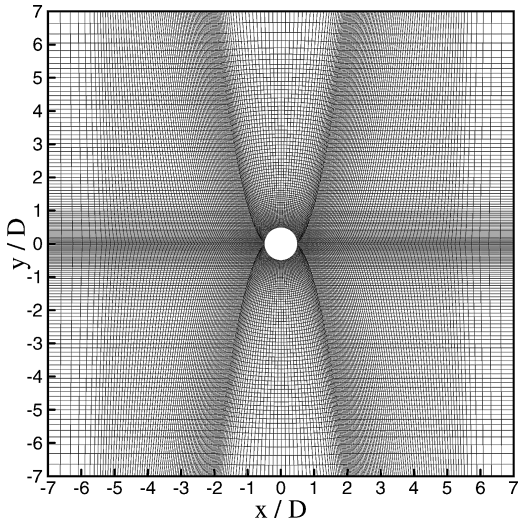

Fig. 1 H-topology grid for calculating inviscid flow past a circular cylinder.

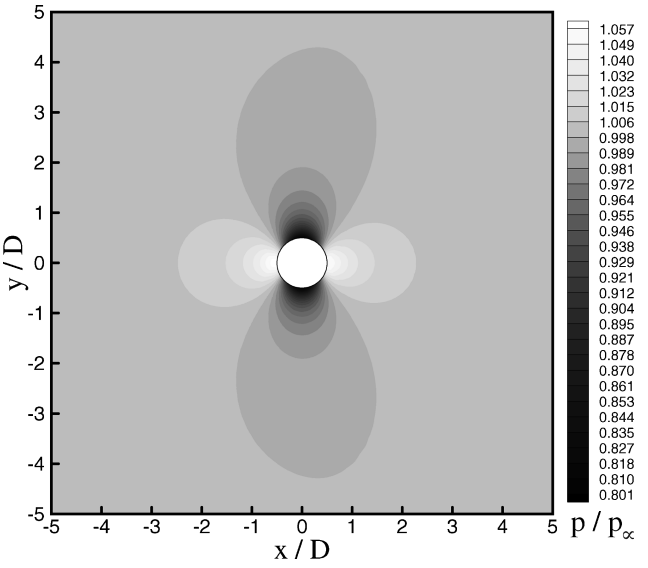

a) Pressure

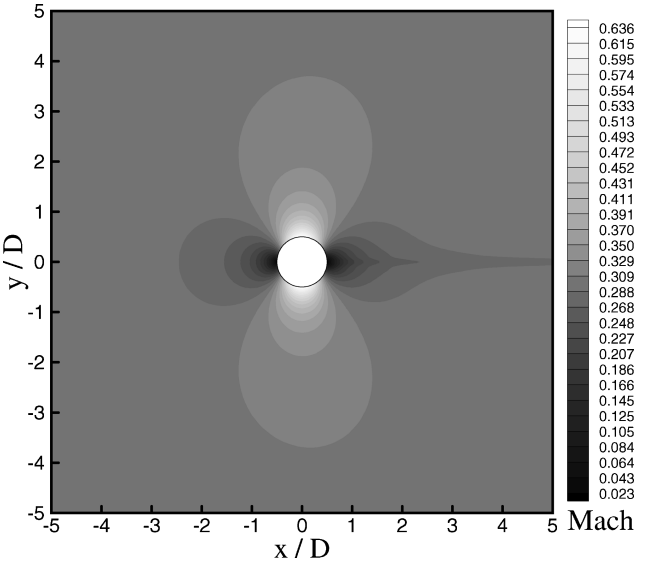

b) Mach number contours

Fig. 2 Steady inviscid flow past a circular cylinder for $M_\infty = 0.3$.

A pressure contour plot in steady state for $M_\infty = 0.3$ is presented in Fig. 2. The pressure coefficient curves in steady state are shown in Fig. 3 along the cylinder surface in comparison with the potential curve given by $C_p = 1 - 4\sin^2\theta$, where θ is measured from the axis of the freestream direction. From Figs. 2 and 3, it is shown that the steady mean solutions are very similar to the potential field of an ideal flow. Based on the steady mean solutions, the dipole sound fields are generated by the pulsating wall boundary conditions. Contour plots of the acoustic pressure $p'(\boldsymbol{x}, t) = p(\boldsymbol{x}, t) - p_{\text{mean}}(\boldsymbol{x})$ at an instance are presented in Fig. 4 for the cases of $M_\infty = 0$ and 0.3. For the zero-Mach-number case, the mean pressure is naturally given by the ambient pressure in the entire domain: $p_{\text{mean}}(\boldsymbol{x}) = p_\infty$. In Fig. 4, it is shown that the dipole sound fields are clearly generated by the proposed wall boundary conditions. The propagation pattern of sound waves is biased in the direction of mean flow, while it is completely symmetric without mean flow.

To compare the calculated solutions with the analytic solution quantitatively, the directivity patterns of SPL at the distance of $r/D = 5$ are given in Fig. 5. It is revealed that the calculated solution of the zero-Mach-number case is in good agreement with the analytic solution. The directivity pattern deviates from the analytic solution as the Mach number increases due to the mean-flow effect, as expected. It is shown that the proposed inviscid wall boundary

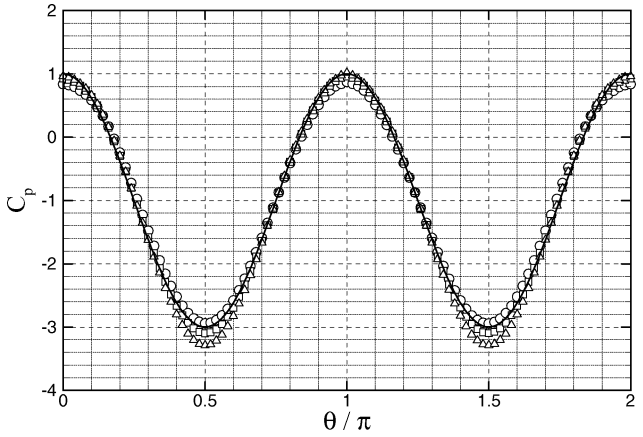

Fig. 3 Pressure coefficient curves along cylinder surface in steady inviscid flow: ——, potential case; ○, $M_\infty = 0.1$; □, $M_\infty = 0.2$; and △, $M_\infty = 0.3$.

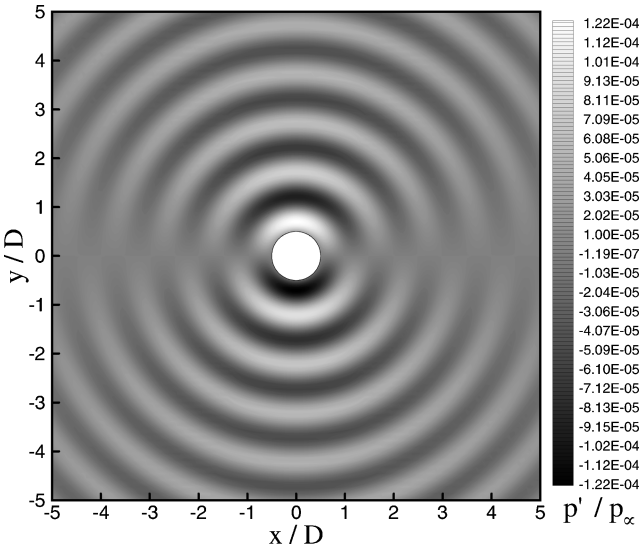

a) $M_\infty = 0$

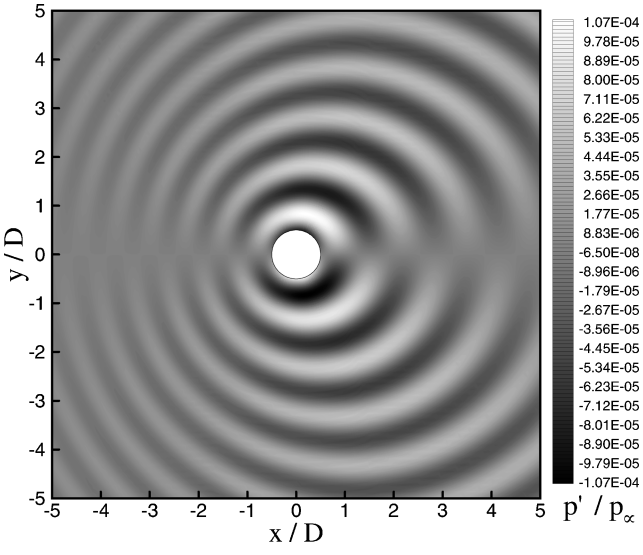

b) $M_\infty = 0.3$

Fig. 4 Visualization of dipole sound fields around an inviscid cylinder by acoustic pressure contours.

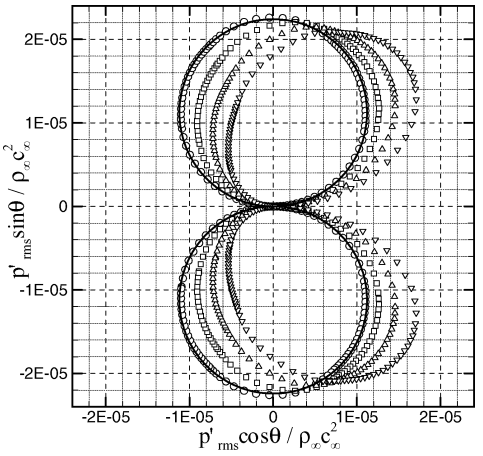

Fig. 5 Directivity patterns of SPLs around an inviscid cylinder at $r/D = 5$: ——, analytic estimation without mean flow; present calculations for the cases of ○, $M_\infty = 0$; □, $M_\infty = 0.1$; △, $M_\infty = 0.2$; and ∇, $M_\infty = 0.3$.

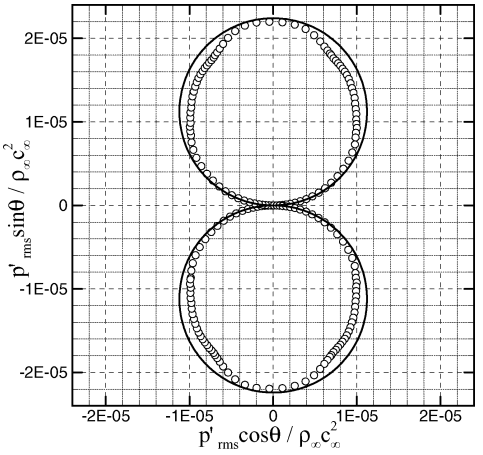

Fig. 6 Result of losing multidimensionality; directivity patterns of SPLs around an inviscid cylinder without mean flow at $r/D = 5$: ——, analytic estimation and ○, calculation with LODI approximation.

conditions can provide accurate acoustic solutions with and without mean flow. Figure 6 shows that loss of the multidimensionality by neglecting the source terms in Eq. (16), that is, turning back to the LODI approximation, results in degrading the accuracy of solutions in acoustic field. The accuracy might not be degraded so much if an orthogonal grid were used. It is shown that true multidimensionality leads to high-quality of acoustic solutions, even on nonorthogonal grid meshes.

B. Viscous Flow past a Stationary Cylinder

A viscous flow past a circular cylinder produces the well-known von Kármán vortex street behind the cylinder. The regular vortex shedding induces perturbation of lift and drag forces on the cylinder. Unlike the inviscid case, the perturbed forces generate the aeolian-tone dipole sound without the oscillation of the cylinder itself. The radiated dipole SPL can be estimated by an analytic formula, which is directly proportional to the rms fluctuating force per unit length on the cylinder surface, so that

$$p'_{\mathrm{rms}}(\boldsymbol{x}) = \overline{p'^2}^{\frac{1}{2}}(\boldsymbol{x}) = \left(\rho_\infty c_\infty^2 / 4\right)\left\{\left[M_\infty^5 Sr / (r/D)\right]\left[\overline{C_L^2}\sin^2\theta + 4\overline{(C_D - \overline{C_D})^2}\cos^2\theta\right]\right\}^{\frac{1}{2}}$$

where $Sr = f_s D/u_\infty$ is the Strouhal number, that is, the nondimensional shedding frequency.[18] In a regular range of Reynolds numbers from about 6×10^1 to 5×10^3, experimental measurements show that

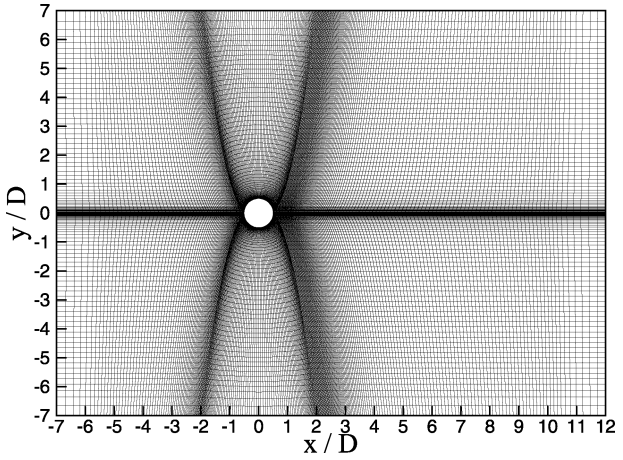

Fig. 7 H-topology grid for calculating viscous flow past a circular cylinder.

the Strouhal number depends only on Reynolds number. The analytic formula does not include the effects of quadrupole sources due to the convection of vortices. It is applicable to the low-subsonic range in which the quadrupole strength is negligible compared with the dipole. It is used to verify the numerical accuracy of the calculated solution.

The von Kármán vortex street and the dipole sound waves are calculated for the case of free-stream Mach number $M_\infty = 0.3$ and Reynolds number $Re_\infty = u_\infty D/\nu_\infty = 4 \times 10^2$. In the literature, it was shown that the street of regularly spaced vortices exists with laminar cores over the range of Reynolds numbers from 65 to approximately 4×10^2 (Ref. 18). Therefore, in this problem, it can be considered that laminar flow is dominant. Equation (1) with the complete viscous term is used in this computation. The grid system used for this problem is shown in Fig. 6. Actually, the same problem was solved in the previous work on orthogonal grid generated by O topology.[1] In the present work, it is challenged on the nonorthogonal grid, as shown in Fig. 7. The number of grid meshes is 272×128. The grid meshes are so concentrated near the cylinder surface that the boundary layer can be captured by about 20 points on average in the radial direction. The smallest grid size is $\Delta x/D = 0.005$ with $\Delta y/D = 0.02$. The grid metrics and Jacobian are evaluated by the numerical differentiation with Eqs. (3–6). The computation is continued until the nondimensional time reaches $u_\infty t/D = 204.0$. The time step size is determined by the CFL condition of Courant number 1.0, and the number of iterations is 200,000.

As a result of the computation, pressure and Mach number contour plots at an instance are presented in Fig. 8 to visualize the von Kármán vortex street. Figure 8 shows the attached boundary layer on the front surface of the cylinder, the mixing layers of the separated flows, and the downstream flow patterns well. The positions of the vortices are revealed clearly. The Strouhal number of periodic vortex shedding can be measured by evaluating the frequency of oscillating lift and drag forces. Time-dependent signals of the lift and drag coefficients are presented in Fig. 9. Those forces are calculated by integrating the distributions of pressure and viscous stresses on the cylinder surface. As shown in Fig. 9, after a transient state due to impulsive initial conditions, a constant frequency and constant magnitudes of the fluctuations are acquired in the periodic shedding mode. The calculated values of Strouhal number, mean drag coefficient, and rms fluctuating drag and lift coefficients are listed in Table 2 compared with the experimental data obtained in low-speed flows of $Re_\infty = 4 \times 10^2$ (Refs. 16 and 18). The results of the calculation with the LODI approximation in the wall boundary conditions also are listed in Table 2. In both cases, using the proposed wall boundary conditions or the previous version of LODI approximation, the mean flow properties are not notably affected and agree well with the experimental data. It can be deduced that the traditional characteristic wall boundary conditions are fair enough to calculate mean flowfields. However, the acoustic fields show different patterns as will be explained.

Table 2 Comparison of Strouhal number, mean drag coefficient, and rms fluctuating drag and lift coefficients

Case	Sr	$\overline{C_D}$	$\overline{(C_D - \overline{C_D})^2}^{\frac{1}{2}}$	$\overline{C_L}^{\frac{1}{2}}$
Experimental data	0.21 ± 0.005	1.2 ± 0.1	——	0.6 ± 0.1
Present results	0.210	1.216	4.209×10^{-2}	0.622
LODI approximation	0.210	1.220	4.179×10^{-2}	0.623

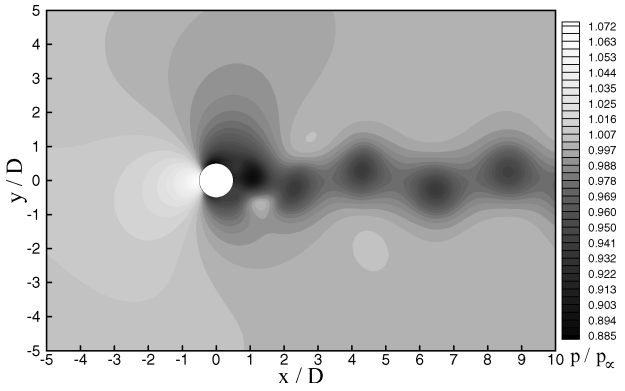

a) Pressure

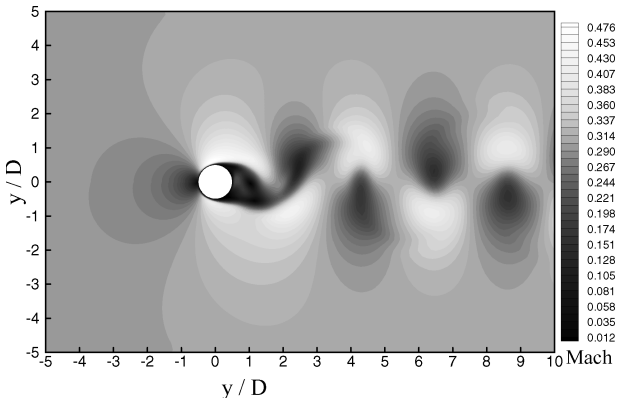

b) Mach number contours

Fig. 8 Visualization of von Kármán vortex street past a circular cylinder for $Re_\infty = 400$ and $M_\infty = 0.3$.

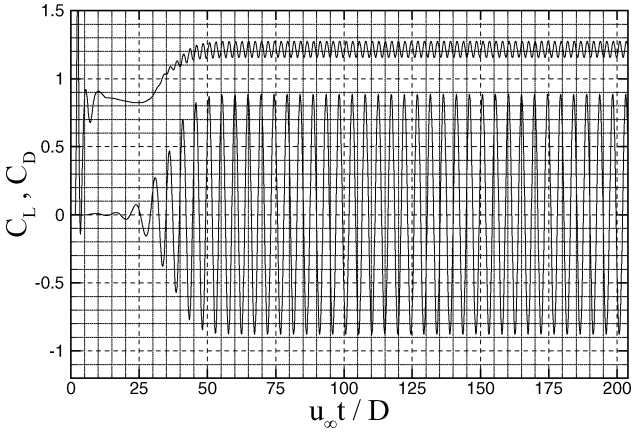

Fig. 9 Time-dependent signals of lift and drag coefficient.

The directivity pattern of SPL produced directly by measuring far-field pressure fluctuations is compared with that estimated by the analytic formula at the distance of $r/D = 5$ in Fig. 10. The analytic formula uses the calculated values of Strouhal number and the rms fluctuating force coefficients. The results of the present computation are in good agreement with the experimental and analytic results. It is shown that the proposed viscous wall boundary conditions can provide accurate aerodynamic and acoustic solutions.

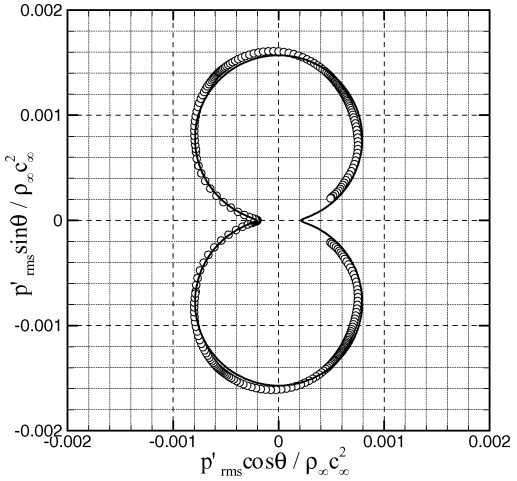

Fig. 10 Directivity patterns SPLs around a viscous cylinder at $r/D = 5$: ——, analytic estimation and ○, present calculation.

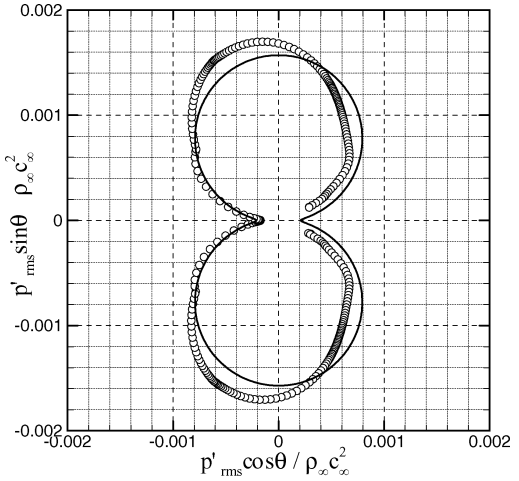

Fig. 11 Result of losing multidimensionality: directivity patterns SPLs around a viscous cylinder at $r/D = 5$: ——, analytic estimation and ○, calculation with LODI approximation.

However, just like the inviscid case, the LODI approximation, neglecting the source terms in Eq. (17) and skipping Eqs. (19) and (20), results in degrading the accuracy of solutions in acoustic field, as shown in Fig. 11. The accuracy might not be degraded as much if an orthogonal grid were used, as was shown in the previous work.[1] Once again, it is demonstrated that true multidimensionality leads to high-quality acoustic solutions, even on nonorthogonal grid meshes.

VI. Conclusions

The generalized characteristic relations are successfully applied to develop accurate wall boundary conditions for various CAA problems. True multidimensionality is fulfilled beyond the LODI approximation by maintaining all of the terms of the original governing equations in the derivation. Mathematically exact and simple expressions of the wall boundary conditions are achieved. Additional conditions for correcting the viscous terms are newly derived. In practice, any kind of extrapolation used by the traditional approach is not needed in the present work. The mathematical exactness of the proposed wall boundary conditions leads to high numerical accuracy in the actual applications. The high-quality aeroacoustic solutions are acquired on nonorthogonal grids due to the guaranteed true multidimensionality. It is shown that the present approach is feasible for application to steady/unsteady and inviscid/viscous CAA problems without difficulties. Further tests and applications to various problems are desirable to verify the generality of the proposed wall boundary conditions in future studies.

Appendix: Transformation Matrices and Constituting Variables

The transformation matrices between the conservative and the characteristic variables and their constituting variables are given as follows:

$$\underline{\boldsymbol{P}}^{-1} = \begin{pmatrix} \boldsymbol{B}_0 \cdot \boldsymbol{l}_x & (\gamma-1)\frac{u}{c^2}\tilde{\xi}_x & (\gamma-1)\frac{v}{c^2}\tilde{\xi}_x + \frac{\tilde{\xi}_z}{\rho} & (\gamma-1)\frac{w}{c^2}\tilde{\xi}_x - \frac{\tilde{\xi}_y}{\rho} & -\frac{\gamma-1}{c^2}\tilde{\xi}_x \\ \boldsymbol{B}_0 \cdot \boldsymbol{l}_y & (\gamma-1)\frac{u}{c^2}\tilde{\xi}_y - \frac{\tilde{\xi}_z}{\rho} & (\gamma-1)\frac{v}{c^2}\tilde{\xi}_y & (\gamma-1)\frac{w}{c^2}\tilde{\xi}_y + \frac{\tilde{\xi}_x}{\rho} & -\frac{\gamma-1}{c^2}\tilde{\xi}_y \\ \boldsymbol{B}_0 \cdot \boldsymbol{l}_z & (\gamma-1)\frac{u}{c^2}\tilde{\xi}_z + \frac{\tilde{\xi}_y}{\rho} & (\gamma-1)\frac{v}{c^2}\tilde{\xi}_z - \frac{\tilde{\xi}_x}{\rho} & (\gamma-1)\frac{w}{c^2}\tilde{\xi}_z & -\frac{\gamma-1}{c^2}\tilde{\xi}_z \\ \frac{c}{\rho}\left(\frac{\gamma-1}{2}M^2 - \frac{\boldsymbol{v}\cdot\boldsymbol{l}_\xi}{c}\right) & \boldsymbol{C}_+ \cdot \boldsymbol{l}_x & \boldsymbol{C}_+ \cdot \boldsymbol{l}_y & \boldsymbol{C}_+ \cdot \boldsymbol{l}_z & \frac{\gamma-1}{\rho c} \\ \frac{c}{\rho}\left(\frac{\gamma-1}{2}M^2 + \frac{\boldsymbol{v}\cdot\boldsymbol{l}_\xi}{c}\right) & \boldsymbol{C}_- \cdot \boldsymbol{l}_x & \boldsymbol{C}_- \cdot \boldsymbol{l}_y & \boldsymbol{C}_- \cdot \boldsymbol{l}_z & \frac{\gamma-1}{\rho c} \end{pmatrix}$$

$$\boldsymbol{B}_0 = \left(1 - \frac{\gamma-1}{2}M^2\right)\boldsymbol{l}_\xi - \frac{1}{\rho}(\boldsymbol{v}\times\boldsymbol{l}_\xi), \qquad \boldsymbol{C}_\pm = \pm\frac{\boldsymbol{l}_\xi}{\rho} - \frac{\gamma-1}{\rho c}\boldsymbol{v}, \qquad \boldsymbol{v} = (u, v, w)^T$$

$$\underline{\boldsymbol{P}} = \begin{pmatrix} \tilde{\xi}_x & \tilde{\xi}_y & \tilde{\xi}_z & \frac{\rho}{2c} & \frac{\rho}{2c} \\ u\tilde{\xi}_x & u\tilde{\xi}_y - \rho\tilde{\xi}_z & u\tilde{\xi}_z + \rho\tilde{\xi}_y & \frac{\rho}{2c}(u + \tilde{\xi}_x c) & \frac{\rho}{2c}(u - \tilde{\xi}_x c) \\ v\tilde{\xi}_x + \rho\tilde{\xi}_z & v\tilde{\xi}_y & v\tilde{\xi}_z - \rho\tilde{\xi}_x & \frac{\rho}{2c}(v + \tilde{\xi}_y c) & \frac{\rho}{2c}(v - \tilde{\xi}_y c) \\ w\tilde{\xi}_x - \rho\tilde{\xi}_y & w\tilde{\xi}_y + \rho\tilde{\xi}_x & w\tilde{\xi}_z & \frac{\rho}{2c}(w + \tilde{\xi}_z c) & \frac{\rho}{2c}(w - \tilde{\xi}_z c) \\ \boldsymbol{b}\cdot\boldsymbol{l}_x & \boldsymbol{b}\cdot\boldsymbol{l}_y & \boldsymbol{b}\cdot\boldsymbol{l}_z & \frac{\rho}{2c}(H + c\boldsymbol{v}\cdot\boldsymbol{l}_\xi) & \frac{\rho}{2c}(H - c\boldsymbol{v}\cdot\boldsymbol{l}_\xi) \end{pmatrix}, \qquad \boldsymbol{b} = \frac{|\boldsymbol{v}|^2}{2}\boldsymbol{l}_\xi + \rho(\boldsymbol{v}\times\boldsymbol{l}_\xi), \qquad H = \frac{|\boldsymbol{v}|^2}{2} + \frac{c^2}{\gamma-1}$$

where $\boldsymbol{l}_x$, $\boldsymbol{l}_y$, and $\boldsymbol{l}_z$ are the unit vectors in the x, y, and z directions, respectively, and $\boldsymbol{l}_\xi$ is the unit normal vector defined by Eq. (10) in Sec. IV.A.

References

[1]Kim, J. W., and Lee, D. J., "Generalized Characteristic Boundary Conditions for Computational Aeroacoustics," *AIAA Journal*, Vol. 38, No. 11, 2000, pp. 2040–2049.

[2]Thompson, K. W., "Time Dependent Boundary Conditions for Hyperbolic Systems," *Journal of Computational Physics*, Vol. 68, No. 1, 1987, pp. 1–24.

[3]Thompson, K. W., "Time Dependent Boundary Conditions for Hyperbolic Systems II," *Journal of Computational Physics*, Vol. 89, No. 2, 1990, pp. 439–461.

[4]Poinsot, T. J., and Lele, S. K., "Boundary Conditions for Direct Simulations of Compressible Viscous Flow," *Journal of Computational Physics*, Vol. 101, No. 1, 1992, pp. 104–129.

[5]Tam, C. K. W., and Dong, Z., "Wall Boundary Conditions for High-Order Finite Difference Schemes in Computational Aeroacoustics," *Theoretical and Computational Fluid Dynamics*, Vol. 6, No. 6, 1994, pp. 303–322.

[6]Kurbatskii, K. A., and Tam, C. K. W., "Cartesian Boundary Treatment of Curved Walls for High-Order Computational Aeroacoustics Schemes," *AIAA Journal*, Vol. 35, No. 1, 1997, pp. 133–140.

[7]Hixon, R., "Curvilinear Wall Boundary Conditions for Computational Aeroacoustics," AIAA Paper 99-2395, June 1999.

[8]Lockard, D. P., and Morris, P. J., "Radiated Noise from Airfoils in Realistic Mean Flows," *AIAA Journal*, Vol. 36, No. 6, 1998, pp. 907–914.

[9]Kim, J. W., and Lee, D. J., "Optimized Compact Finite Difference Schemes with Maximum Resolution," *AIAA Journal*, Vol. 34, No. 5, 1996, pp. 887–893.

[10]Kim, J. W., and Lee, D. J., "Implementation of Boundary Conditions for Optimized High-Order Compact Schemes," *Journal of Computational Acoustics,* Vol. 5, No. 2, 1997, pp. 177–191.

[11]Kim, J. W., and Lee, D. J., "Adaptive Nonlinear Artificial Dissipation Model for Computational Aeroacoustics," *AIAA Journal*, Vol. 39, No. 5, 2001, pp. 810–818.

[12]Freund, J. B., "Proposed Inflow/Outflow Boundary Conditions for Direct Computation of Aerodynamic Sound," *AIAA Journal*, Vol. 35, No. 4, 1997, pp. 740–742.

[13]Warming, R. F., Beam, R. M., and Hyett, B. J., "Diagonalization and Simultaneous Symmetrization of Gas-Dynamic Matrices," *Mathematics of Computation*, Vol. 29, No. 132, 1975, pp. 1037–1045.

[14]Hirsch, C., *Numerical Computation of Internal and External Flows*, 1st ed., Vol. 2, Wiley, New York, 1992, pp. 132–223.

[15]Tourrette, L., "Artificial Boundary Conditions for the Linearized Compressible Navier–Stokes Equations," *Journal of Computational Physics*, Vol. 137, No. 1, 1997, pp. 1–37.

[16]Schlichting, H., *Boundary Layer Theory*, 7th ed., McGraw–Hill, New York, 1979, pp. 24–46.

[17]Dowling, A. P., and Ffowcs Williams, J. E., *Sound and Sources of Sound*, 1st ed., Wiley, New York, 1983, pp. 60, 61.

[18]Blake, W. K., *Mechanics of Flow-Induced Sound and Vibration*, 1st ed., Vol. 1, Academic Press, New York, 1986, pp. 219–287.

W. Devenport
Associate Editor